

Xiaoliang Zhang<sup>1</sup>

Ming Hu<sup>2</sup>

e-mail: hum@ethz.ch

Laboratory of Thermodynamics  
in Emerging Technologies,  
Department of Mechanical and  
Process Engineering,  
ETH Zürich,  
8092 Zürich, Switzerland

Konstantinos P. Giapis

Division of Chemistry and Chemical Engineering,  
California Institute of Technology,  
Pasadena, CA 91125  
e-mail: giapis@cheme.caltech.edu

Dimos Poulikakos

Laboratory of Thermodynamics  
in Emerging Technologies,  
Department of Mechanical and  
Process Engineering,  
ETH Zürich,  
8092 Zürich, Switzerland  
e-mail: dimos.poulikakos@ethz.ch

# Schemes for and Mechanisms of Reduction in Thermal Conductivity in Nanostructured Thermoelectrics

*Nonequilibrium molecular dynamics (NEMD) simulations were performed to investigate schemes for enhancing the energy conversion efficiency of thermoelectric nanowires (NWs), including (1) roughening of the nanowire surface, (2) creating nanoparticle inclusions in the nanowires, and (3) coating the nanowire surface with other materials. The enhancement in energy conversion efficiency was inferred from the reduction in thermal conductivity of the nanowire, which was calculated by imposing a temperature gradient in the longitudinal direction. Compared to pristine nanowires, our simulation results show that the schemes proposed above lead to nanocomposite structures with considerably lower thermal conductivity (up to 82% reduction), implying ~5X enhancement in the ZT coefficient. This significant effect appears to have two origins: (1) increase in phonon-boundary scattering and (2) onset of interfacial interference. The results suggest new fundamental–yet realizable ways to improve markedly the energy conversion efficiency of nanostructured thermoelectrics. [DOI: 10.1115/1.4006750]*

*Keywords:* Si nanowire, core-shell, thermal conductivity, thermoelectric materials, molecular dynamics

## 1 Introduction

Thermoelectric materials can directly convert heat to electricity and vice versa, offering a promising approach to waste-heat recovery. The energy conversion efficiency of thermoelectric devices depends on  $ZT$ , a dimensionless coefficient defined as  $ZT = S^2\sigma T/\kappa$ , where  $S$ ,  $\sigma$ ,  $T$ , and  $\kappa$  are the Seebeck coefficient, electrical conductivity, absolute temperature, and thermal conductivity of the material, respectively. A large  $ZT$  value signifies a more efficient thermoelectric, though it has been challenging to increase  $ZT$  because  $S$ ,  $\sigma$ , and  $\kappa$  are interdependent [1].

It has been shown in experiments that the thermal conductivity of individual Si nanowires is more than two orders of magnitude lower than that of bulk Si, due to increased phonon-boundary scattering and possible phonon spectrum modification [2]. The Seebeck coefficient and electrical conductivity of Si nanowires, 50 nm in diameter, are almost the same as those of bulk Si [3]. Ab initio calculations suggest that these properties should remain invariant even for diameters as small as 2 nm [4]. Thus, lowering the thermal conductivity can have a direct effect on  $ZT$ : Nanowires with diameters of ~50 nm should have  $ZT \sim 0.6$  at room temperature [3], high enough to render Si nanowires promising for thermoelectric conversion.

For larger thermoelectric efficiency, nanostructuring has emerged as an alternative way to further reduce the thermal conductivity of Si nanowires by increasing phonon scattering and phonon interference. For example, coating of discrete 5–10 nm platinum nanoparticles on the surface of high-density, aligned,  $n$ -type silicon nanowire solar cells yielded a substantial enhancement in energy conversion efficiency [5]. Doped with 50% isotope

atoms, the thermal conductivity of pure Si nanowire can be lowered by 73%, caused by mismatch in phonon spectra [6]. Using molecular dynamics simulations, it was shown that a Ge layer (shell) of only 1 to 2 unit cells in thickness on a single-crystalline Si nanowire can lead to a dramatic 75% decrease in thermal conductivity at room temperature compared to an uncoated Si nanowire [7,8].

In this paper, we employ NEMD simulations to investigate three schemes for reducing the thermal conductivity of Si NWs: (1) roughening of the NW surface, (2) incorporating nanoparticles into NWs, and (3) coating the NW surface with other materials. The thermal conductivity of the Si NW is calculated by imposing a one-dimensional temperature gradient in the longitudinal direction. Based on calculations of the phonon density of states and the participation ratio of each phonon mode, we propose a common underlying mechanism to explain the reduction in thermal conductivity.

The remainder of this paper is organized as follows: In Sec. 2, we present the three different model structures considered and describe the interatomic potential and the MD methodology used to determine the thermal conductivity of the nanowires. In Sec. 3, we present the results and discuss the mechanisms for the reduction in thermal conductivity of the Si core. Finally, the main points are summarized in Sec. 4.

## 2 Model Structures and Simulation Procedure

**2.1 Model Structures.** We investigated three types of Si NW structures: (1) a Si rod covered with W particles, (2) a Si rod with inclusions, and (3) a Si-core coated with various materials. For all cases studied, a square cross-sectional Si core was constructed from diamond-structured bulk silicon with  $n \times n \times m$  unit cells (where  $m$  is much larger than  $n$ ) in the  $x$ ,  $y$ , and  $z$  directions. We took the lattice constant of Si as 0.357 nm. The NW extends in the [001] direction, which is set along the  $z$ -axis. The surfaces

<sup>1</sup>Permanent address: Center for Heat and Mass Transfer, Institute of Engineering Thermophysics, Chinese Academy of Sciences, Beijing 100190, China; Graduate School of Chinese Academy of Sciences, Beijing 100049, China.

<sup>2</sup>Corresponding author.

Contributed by the Heat Transfer Division of ASME for publication in the JOURNAL OF HEAT TRANSFER. Manuscript received June 22, 2011; final manuscript received April 21, 2012; published online August 6, 2012. Assoc. Editor: Robert D. Tzou.

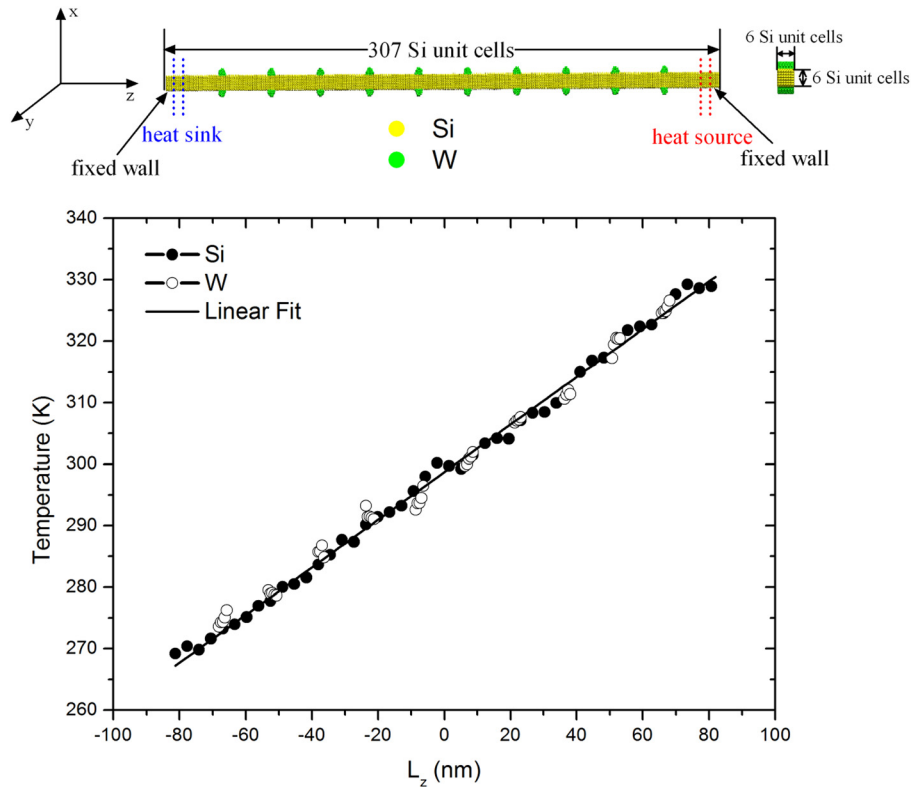


**Fig. 1 (Top) Side and cross-sectional view of the Si-W nanowire with  $6 \times 6 \times 307$  unit cells of Si nanowire covered by 10 W particles. Color coding: gray, Si; dark, W. (Bottom) The corresponding temperature profiles for the Si core and W particles. The solid line is a linear fit to the temperature profile of the Si core.**

in transverse directions ( $x$ -axis and  $y$ -axis) are of (110)-type for all structures.

For Si NW covered with W particles, the Si nanowire is single-crystalline with  $6 \times 6 \times 307$  unit cells, corresponding to a cross-sectional width of 2.3 nm and a length of 167 nm. The nanowire surface is covered by different numbers of W particles ranging from 20 to 100, corresponding to a surface coverage from 7.34% to 36.7%. After constructing the Si NW, bcc W particles with lattice constant of 3.162 Å, were built on each  $y$ - $z$  surface with the same orientation as the Si NW. Ten half-cylinder-like particles with radius of 1.086 nm and height of 2.3 nm were regularly placed on each  $y$ - $z$  surface of the Si NW, as shown in the top panel of Fig. 1. The positions of the W particles are between  $-74$  nm and  $+74$  nm along the  $z$  direction of the Si NW, which is the region used later to compute the heat flux upon applying a temperature gradient. A random placement of the W particles helped check the sensitivity of the thermal conductivity results to the particle configuration. For Si NW with inclusions, we first selected several spherical regions with radius of 2 Si unit cells inside the Si NW ( $n \times n \times 302$ ,  $n=9, 16$ ) along the longitudinal direction. The structure was constructed either by replacing Si atoms in these regions with some other type of atoms, e.g., Ge, or by changing the atom mass to a different values, e.g., 2, 4, and 8 times larger, or by modifying the interatomic interaction strength, e.g., eight times larger to mimic diamond particles. For core-shell nanowires, the Si core was also single crystalline with  $6 \times 6 \times 307$  unit cells (167 nm long). In this work, we investigated different materials as the shell, including single-crystalline SiC, GaN, and AlN, as all of these crystalline lattices can be grown on Si substrate in experiments [9–11]. All crystalline shells are zinc-blende structures. To study the effect of crystallinity of the shell structure on the thermal conductivity of the Si core, we also built amorphous SiC layer on the Si core, by heating the SiC crystalline up to 3000 K to melt it and then quenching it down to 300 K very fast. Furthermore, the

thermal conductivity of Si core coated by amorphous SiO<sub>2</sub> and Si<sub>3</sub>N<sub>4</sub> are also investigated, both of which are obtained by the same procedure as the amorphous SiC.

**2.2 Interatomic Potential.** For Si-W system, the improved Tersoff potential, named the MOD potential [12], was used to describe the Si-Si interactions in Si NW, which can reproduce the elastic constants and melting point of diamond silicon as well as the cohesive energies and equilibrium bond lengths of silicon polytypes. An analytical interatomic potential for modeling nonequilibrium processes in the W-C-H system [13] was used to describe the W-W interactions in W particles. To describe the Si-W interactions, we transformed the W-W Tersoff-type parameters to MOD type. Parameters for Si-W interactions were obtained by taking the arithmetic mean of Si and W parameters for  $(\lambda_1)_{\text{Si-W}}$  and  $(\lambda_2)_{\text{Si-W}}$  and the geometric mean for  $A_{\text{Si-W}}$ ,  $B_{\text{Si-W}}$ ,  $(R_1)_{\text{Si-W}}$ , and  $(R_2)_{\text{Si-W}}$  as suggested by Tersoff [14]. For other parameters, we obtained  $\beta_{\text{Si-W}}$ ,  $h_{\text{Si-W}}$ ,  $\eta_{\text{Si-W}}$ , and  $(\eta \times \delta)_{\text{Si-W}}$  from the arithmetic mean and  $\alpha_{\text{Si-W}}$ ,  $(c_i, i=1 \dots 5)_{\text{Si-W}}$  from the geometric mean.

For Si NW with inclusions, the Stillinger-Weber potential was used to describe the interactions in the Si-NW/Ge-inclusions system with diamond structure. This potential uses two-body and three-body terms to stabilize the diamond lattice. The original parameters were developed to provide an approximate description of condensed phases of Si [15]. Parameters for Ge were determined by fitting to experimental data [16]. In the simulation studies described herein, the parameters of Refs. [15] and [16] were adopted to describe Si-Si and Ge-Ge interactions. Parameters for Si-Ge interactions were obtained by taking the arithmetic mean of Si and Ge parameters for  $\sigma_{\text{Si-Ge}}$  and the geometric mean for  $\lambda_{\text{Si-Ge}}$  and  $\epsilon_{\text{Si-Ge}}$ , as suggested in the literature [17].

For Si nanowires coated with crystalline SiC, GaN, and AlN, the Si core was also modeled with the MOD potential [12]. An

optimized analytical bond-order potential [18] was used to describe both the crystalline and amorphous SiC shell. Elastic properties of the dimer as well as solid phases SiC are very well reproduced by this potential. In addition, point defect formation enthalpies show good agreement with first-principles calculations. An analytical bond-order potential [19], which describes a wide range of structural properties of GaN as well as bonding and structure of the pure constituents, was used to model the GaN shell. The same potential was used by Zhou and Jones [20] to simulate thermal conductivity of GaN system. For AlN, we used the modified Tersoff potential [21], which is in good agreement with the experimental values for structural and elastic properties of group III-Nitrides. Al–Al Tersoff parameters were taken from Ref. [22] and N–N parameters are the same as that in GaN parameters [19]. Using the mixing rule as in Si–W case, we transformed the non-MOD Tersoff parameters to the MOD-type and combined them with the Si MOD parameters to describe the interatomic interactions between the Si core and the shell material. A modified parameter set of the Tersoff potential [23], fitted to ab initio calculations and experimental data, was used to investigate the thermal conductivity of Si/amorphous SiO<sub>2</sub> core–shell nanowire. Interatomic interactions for Si/Si<sub>3</sub>N<sub>4</sub> were described by an ab initio derived augmented Tersoff potential [24,25], which has been used previously to study the structural features and the coordination defects of amorphous SiN<sub>x</sub> samples at various stoichiometries [26].

**2.3 Simulation Procedure.** All MD calculations were performed using the LAMMPS [27] package with a time step of 1 fs throughout. Free boundary conditions are used in transverse directions. We set 1.5 nm long regions at both ends as “rigid wall.” In the first stage of MD simulations, we relaxed the system at 300 K for 0.5 ns with the walls moving freely along the longitudinal direction, corresponding to zero pressure, using Nosé-Hoover thermostat [28,29]. After NVT relaxation, we froze the walls and continued to relax the system with NVE ensemble for another 0.5 ns.

Following equilibration, we computed the thermal conductivity of the system using nonequilibrium MD. It is well known that, using nonequilibrium molecular dynamics to compute thermal conductivity relies on a steady heat flux, which must be established along the desired direction. Currently, there are two different methods to realize this: (1) constant heat flux, e.g., the Jund and Julien algorithm [30] or the Müller-Plathe algorithm [31] in which the heat current or flux is an input parameter and the resulting temperature gradient is calculated; (2) constant temperature gradient, i.e., heat source and heat sink are connected to constant temperature thermostats (thus, the temperature gradient is known in advance) and the resulting heat flux is calculated. In our simulation, we adopted the second method. To establish a temperature gradient along the longitudinal direction, we set another 3 nm long region next to the wall as heat source and heat sink. The temperature gradient is realized by using Nosé-Hoover thermostats to keep the temperature of heat source and heat sink at 310 K and 290 K, respectively, corresponding to a typical temperature gradient of  $\sim 0.1 \pm 0.002$  K/nm, which is far less than the limits in Ref. [32]. We calculated the heat flux along the longitudinal direction according to the following expression [32]:

$$J_L(t) = \frac{1}{V} \left[ \sum_i v_{i,L} \varepsilon_i + \frac{1}{2} \sum_{i,j,i \neq j} r_{ij,L} (\vec{f}_{ij} \cdot \vec{v}_j) + \sum_{i,j,k} r_{ij,L} (\vec{f}_j(ijk) \cdot \vec{v}_j) \right] \quad (1)$$

where the subscript “L” denotes a quantity in the longitudinal direction;  $v_i$  is the velocity of atom  $i$ ;  $\varepsilon_i$  is the local site energy;  $r_{ij}$  is the relative distance between atom  $i$  and  $j$ ;  $\vec{f}_{ij}$  is the two-body force between atom  $i$  and  $j$ ;  $\vec{f}_j(ijk)$  is the three-body interactions between atoms  $i$ ,  $j$ , and  $k$ ; and  $V$  is the volume of the region

selected to calculate the heat flux. Note that we exclude the regions ( $\sim 10$  unit cells long) close to both ends and compute the heat current only for the rest of the nanowire to avoid the nonlinear effect of the heat source and heat sink at the ends. The thermal conductivity of the nanowire is calculated from

$$\kappa = -\frac{\vec{J}_L}{\partial T / \partial z} \quad (2)$$

where  $\vec{J}_L$  is the averaged heat flux in the longitudinal direction and  $\partial T / \partial z$  is the temperature gradient determined from a linear fitting of the time-averaged temperature profile along the nanowire, as shown in the bottom panel of Fig. 1. For selected cases, we compared the results to those obtained using the Müller-Plathe algorithm and found them to be similar, especially pertaining to the reduction in thermal conductivity. A typical heat-source heat-sink run took about 10 ns to establish steady heat flow and an additional 10–20 ns for averaging the temperature profile and heat flux, depending on system size and its thermal conductivity.

### 3 Results and Discussion

**3.1 Si Nanowire Decorated With W Particles.** The calculated thermal conductivity of Si NW decorated with W particles, plotted in Fig. 2, is found to largely decrease as the W-particle coverage increases. Notably, a W surface coverage of 15% decreases the thermal conductivity of the Si core by over 50%. Larger W coverage helps to reduce the core conductivity further, approaching asymptotically a reduction value of  $\sim 70\%$ . Importantly, the thermal conductivity of the Si core does not change much when the W particle distribution becomes random. Since epitaxial growth of islands of another material on Si NW surfaces has been realized experimentally [33], the present method of reducing the thermal conductivity of the core appears promising. We note the discrepancy between our calculated thermal conductivity and the experimental value [2]. The difference can be attributed to defects, impurities, surface roughness, and oxidation, which are always present in the experimental samples and may impact adversely the nanowire’s thermal conductivity. In contrast, theoretical calculations assume that the Si nanowires are perfect crystals with atomically smooth surfaces, which facilitate heat conduction. Despite this discrepancy, the predicted reduction in thermal conductivity is still valid and is the main point of this paper.

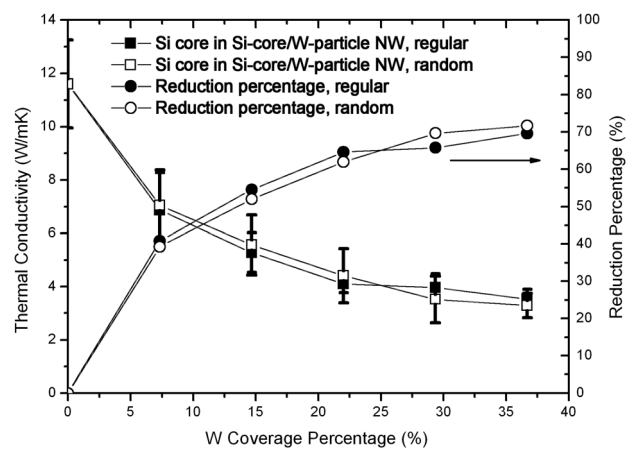


**Fig. 2 Thermal conductivity of  $6 \times 6 \times 307$  u.c. (167 nm long) Si core in Si–W nanowire as a function of W coverage percentage with 0% denotes pure Si NW. The right axis is the reduction percentage of the thermal conductivity of the Si core in the Si/W NW relative to that of pure Si NW, as indicated by the arrow. Filled and empty symbols are for Si–W NW with regular and random W particles, respectively.**

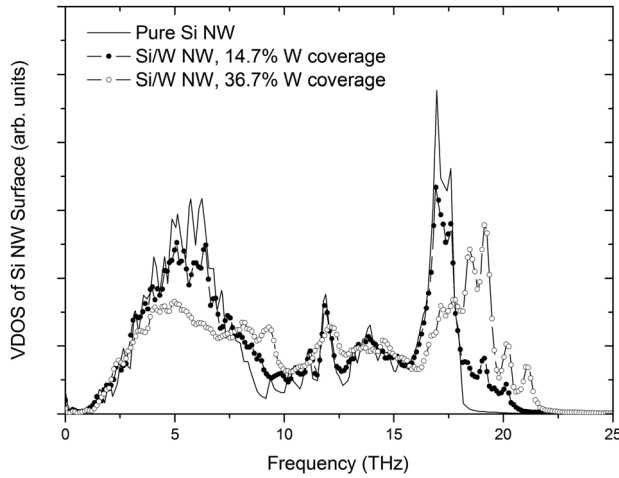


**Fig. 3 Comparison of vibrational density of states of Si atoms on the surface of Si–W nanowire with different W coverages**

The significant reduction is attributed to the depression in the vibrational density of states (VDOS) of Si atoms on the nanowire surface upon addition of the W particles. The VDOS, plotted in Fig. 3, is calculated by a Fourier transform of the atomic velocity autocorrelation function. Addition of the W particles not only results in a large attenuation of the low-frequency modes, especially below 7.5 THz but also in a large drop in the high frequency modes around 17 THz. This is caused by phonon interference at the Si/W NW interface emanating from the lattice mismatch and the large atomic mass difference between Si and W, which enhance phonon scattering. Since low-frequency modes dominate heat transfer in the Si core, their attenuation impacts adversely the thermal conductivity. It is worth pointing out that, the VDOS of Si atoms not in contact with the W particles, (as well as those in the center of the Si core) does not change much with the addition of W particles (not shown for brevity). That is, only the vibrations of the Si atoms in contact with the W particles are affected. It is worth noting that, at larger W coverage, the high frequency modes of Si shift to higher frequencies. This can be attributed to the strong confinement effect due to the high frequency W modes [34–36].

Furthermore, we analyzed the phonon mode localization by calculating the mode participation ratio  $p_\lambda$ , defined for each mode  $\lambda$  as [37]

$$p_\lambda^{-1} = N \sum_i \left( \sum_\alpha \varepsilon_{i\alpha,\lambda}^* \varepsilon_{i\alpha,\lambda} \right)^2 \quad (3)$$

where  $i$  sums the overall atoms studied,  $\alpha$  is a Cartesian direction and sums over  $x, y, z$ ,  $\varepsilon_{i\alpha,\lambda}$  the vibrational eigenvector component corresponding to the  $\lambda$ th normal mode, and  $N$  is the total number of atoms. The participation ratio describes the fraction of atoms participating in a particular mode and, hence, it varies between  $O(1)$  for delocalized states to  $O(1/N)$  for localized states. First, we selected a segment of  $6 \times 6 \times n$  ( $n = 1, 2, 5, 7, 9, 14$ ) Si NW, the longitudinal length of NW ranging from 0.543 nm to 7.602 nm, and mimic the infinitely long NW by using periodic boundary conditions in the longitudinal direction, and we found that the participation ratio did not change as the length of Si NW increases. In order to compute the participation ratio of Si/W NW as a function of W coverage, we took 14 and 5 Si unit cells long NW covered by one W particle to mimic the cases of Si/W NW with W coverage of 14.7% and 36.7%, respectively.

Figure 4(a) compares the participation ratios of all modes in the spectrum for pure Si NW and the Si/W NWs with different number of W particles. For the pure Si NW, participation ratios are

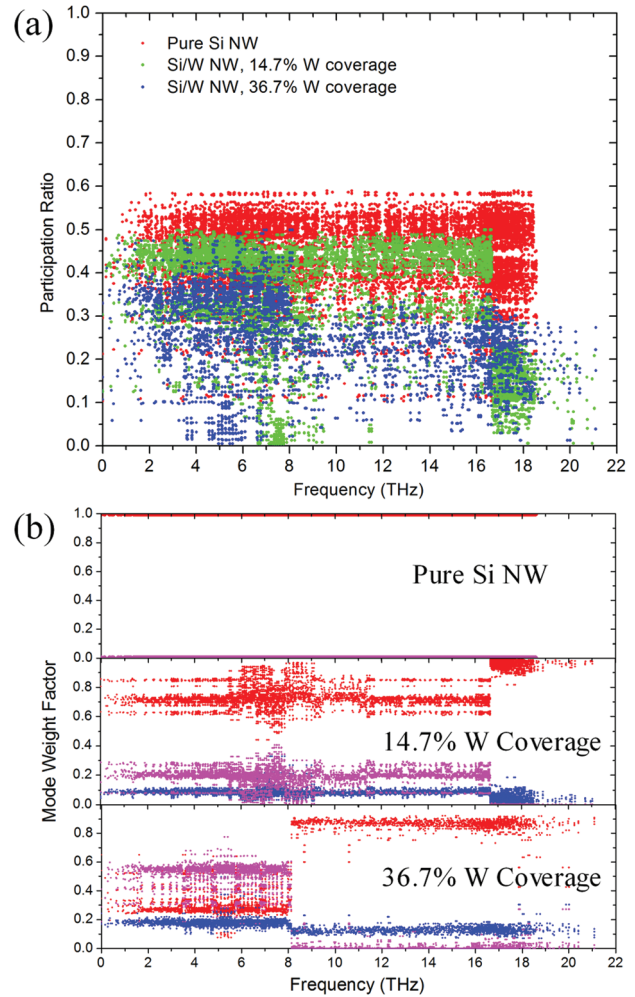


**Fig. 4 Participation ratio (a) and mode weight factor (b) of each vibrational eigen-mode for Si–W nanowires with different W coverages. Color code in (b): red: Si core, blue: Si–W interface, pink: W interior.**

almost uniformly distributed as a function of frequency. For Si/W NW with 14.7% W coverage, the participation ratios of the phonon modes over the entire frequency range are reduced. For the high frequency modes ( $16.7 \text{ THz} < \omega < 18.6 \text{ THz}$ ), in particular, there is a large reduction in the participation ratios. Furthermore, some even higher frequency but more localized modes ( $18.6 \text{ THz} < \omega < 21 \text{ THz}$ ) are excited, which is consistent with the VDOS in Fig. 3. For Si/W NW with 36.7% W coverage, not only are the participation ratios of low frequency ( $\omega < 7.8 \text{ THz}$ ) modes reduced but also the intermediate frequency ( $7.8 \text{ THz} < \omega < 16.7 \text{ THz}$ ) modes become more localized. However, the thermal conductivity of the Si core does not decrease more than in the case of 14.7% W coverage (Fig. 2). This observation suggests that the high frequency modes do not influence heat conduction in the Si/W nanowire as much. Further analysis was provided by the mode weight factor [8] defined as

$$f_{j,\lambda} = \sum_j' \sum_\alpha (\varepsilon_{j\alpha,\lambda})^2 \quad (4)$$

where the prime denotes that sum over  $j$  (atoms). This factor can be evaluated for each region by accounting for only the atoms of that region (the interior of the Si core, the Si–W interface, and the interior of the W particles). The Si–W interfacial region is defined by the Si and W atoms, which have at least one neighbor from the other element within the cutoff distance of the force field.

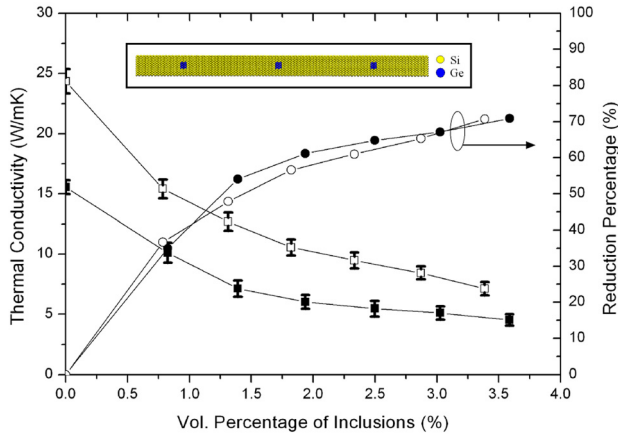


**Fig. 5** Thermal conductivity of  $9 \times 9 \times 302$  u.c. and  $16 \times 16 \times 302$  u.c. ( $164$  nm long) Si nanowire with Ge inclusions as a function of Ge volume percentage with 0% denotes pure Si nanowire. The right axis is the reduction percentage of the thermal conductivity of the Si nanowire with Ge inclusions relative to that of pure Si nanowire, as indicated by the arrow. Filled and open symbols are for the case of  $9 \times 9 \times 302$  u.c. and  $16 \times 16 \times 302$  u.c., respectively. (Inset) A segment of Si nanowire with Ge inclusions. Color coding: gray, Si; dark, Ge.

Consequently, the sum of the mode weight factors in the Si/W nanowire is equal to unity, i.e.,  $f_{\text{core},\lambda} + f_{\text{interface},\lambda} + f_{\text{particle},\lambda} = 1$ . For the different regions studied (Si core, Si–W interface, W interior), the mode weight factor results shown in Fig. 4(b) suggest that the presence of the W particles depresses the vibrations of the Si core significantly and causes the Si core to vibrate resonantly with the W atoms, which corresponds to a confinement effect of the W particles on the vibrational modes of the Si core. The reduction in the thermal conductivity could also be explained by enhanced phonon scattering due to the presence of W particles.

**3.2 Si Nanowire With Inclusions.** For a Si nanowire with inclusions, we first computed the thermal conductivity of the Si NW with different numbers of Ge inclusions. A short segment of Si nanowire with Ge inclusions is shown in the inset of Fig. 5. The thermal conductivity results are reported in Fig. 5, from which we can see that the thermal conductivity of Si-NW/Ge-inclusions drops as the volume percentage of Ge inclusions increases. With about 3.5% volume inclusions, the thermal conductivity drop can be as high as 70%. Remarkably, the thermal conductivity reduction is almost independent of the nanowire cross section (e.g.,  $9 \times 9 \times 302$  and  $16 \times 16 \times 302$  unit cells) for a wide range of volumetric inclusions of Ge. This implies that the drop in thermal conductivity of the Si nanowire can be flexibly controlled by the inclusions. Such inclusions could be easily realized in experiments by sputtering Ge nanoparticles during growth of Si NW.

In order to investigate the effect of different types of inclusions on reducing the thermal conductivity of Si nanowire, we studied nine different materials and computed the resulted thermal conductivity. For all cases, the Si NW is  $9 \times 9 \times 302$  unit cells with nine inclusions of radius 2 Si unit cells. All inclusions are regularly spaced inside the Si nanowire along the longitudinal axis, except where stated otherwise. The results are collected in Fig. 6. In all cases, significant reduction ( $\sim 60$ – $70\%$ ) in thermal conductivity of Si NW was observed, which is the direct result of strong phonon scattering at the inclusion–matrix interface induced by the mass difference between them. By comparing the results of different types of inclusions, we also found that the conductivity reduction levels off as the atomic mass of the inclusion and the interfacial interaction strength increase. On the other hand, the random placement of inclusions can extend this effect, because of

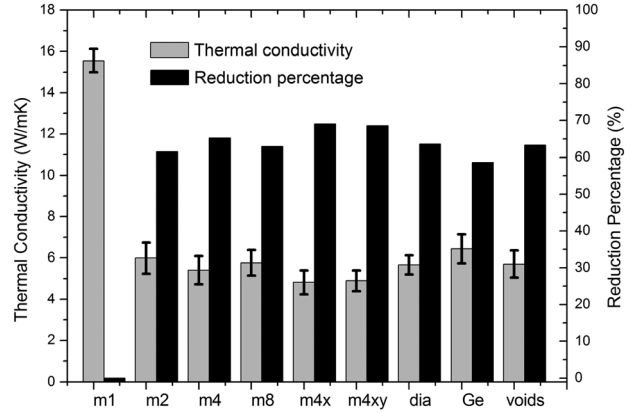


**Fig. 6** Thermal conductivity of Si nanowires with different types of inclusions. For all cases, the Si nanowire is  $9 \times 9 \times 302$  unit cells with nine inclusions and the radius of all inclusions is 2 Si unit cells. “m1”: pure Si nanowire; “m2,” “m4,” “m8”: atom mass in inclusions is 2, 4, and 8 times larger than normal Si, respectively; “m4x” and “m4xy”: same atom mass as “m4” but inclusions are randomly placed in x direction (also y direction for the later) to block the perfect lattice vibrations in that direction; “dia”: normal Si mass but interatomic interaction strength inside inclusions is eight times larger than normal Si (to mimic diamond inclusions); “Ge”: normal Ge inclusions; “voids”: remove atoms in inclusions.

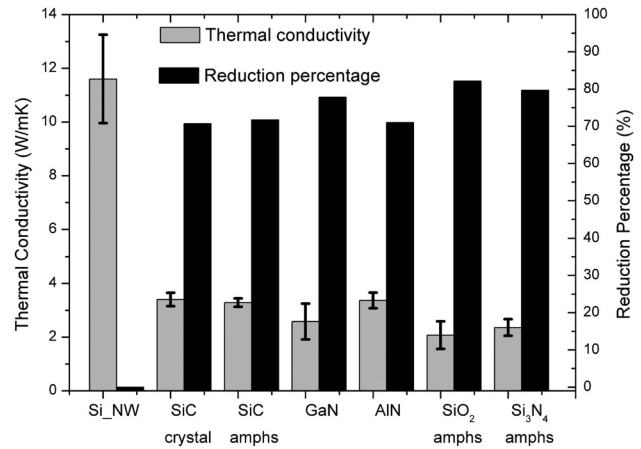


**Fig. 7** Thermal conductivity of Si-based core–shell nanowires with different shell structures. For all cases, the Si core is  $6 \times 6 \times 307$  unit cells. Si\_NW: pure Si nanowire; SiC crystal: Si-core/crystalline-SiC-shell nanowire; SiC amphs: Si-core/amorphous-SiC-shell nanowire; GaN: Si-core/GaN-shell nanowire; AlN: Si-core/AlN-shell nanowire; SiO<sub>2</sub> amphs: Si-core/amorphous-SiO<sub>2</sub>-shell nanowire; Si<sub>3</sub>N<sub>4</sub> amphs: Si-core/amorphous-Si<sub>3</sub>N<sub>4</sub>-shell nanowire.

the enhanced phonon scattering at inclusion–matrix interface, similar as scattering at rough interfaces [38–41].

**3.3 Si-Based Core-Shell Nanowire.** The thermal conductivity of Si-based core–shell nanowires with different types of shell material is plotted in Fig. 7. As reported previously for Ge coated Si nanowires [7,8], a dramatic reduction (over 70%) in the thermal conductivity of the Si core was observed. For crystalline SiC, GaN, and AlN shell structures with the same interatomic potential [12] for Si core, we found that the crystalline GaN shell exhibits an even better performance—a dramatic reduction of 78% in thermal conductivity. This remarkable result can be attributed to two aspects: (1) the strong interaction strength between the GaN shell and Si core surface and (2) the large atomic mass difference

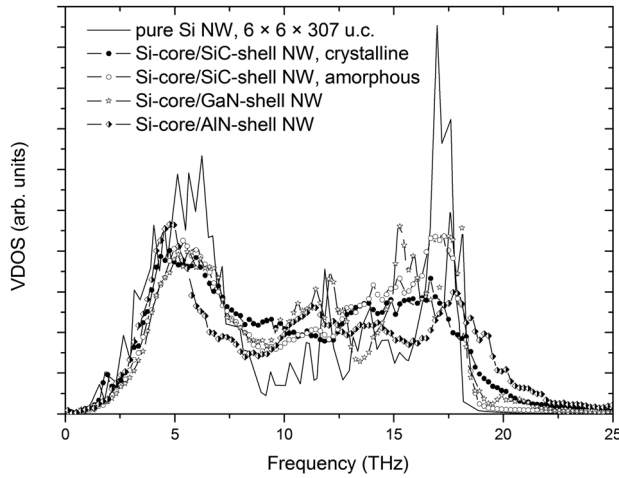


**Fig. 8 Comparison of vibrational density of states of Si atoms on the surface of Si core in Si-based core-shell nanowires with different shell structures**

between Ga and Si. Our calculations show that the interfacial cohesive energy of  $\sim 5.18$  J/m<sup>2</sup> for GaN–Si, is 13.7%, 42.0%, and 57.1% higher than that of crystalline SiC–Si, amorphous SiC–Si, and crystalline AlN–Si, respectively. As we pointed out previously [8], the significant reduction in thermal conductivity of core–shell nanowires is a consequence of phonon interference at the core–shell interface, which, in turn, depends on the interfacial interaction strength. Different shell materials change the degree of coupling between vibrational modes in the core and the shell. When the coupling is strong, phonon interference impedes heat transfer [8]. Regarding the atomic mass difference, it is well known that it influences strongly phonon scattering; thus, it makes sense physically that heavy Ga atoms can bring more significant phonon scattering at the core–shell interface.

We also computed the VDOS of Si atoms on the surface of Si core for the four different shell structures as well as for a pure Si nanowire, which are compared in Fig. 8. It is clearly seen that the VDOS of all four shell structures is largely reduced, both at low ( $\sim 6$  THz) and high ( $\sim 17$  THz) frequencies. This is mainly attributed to the lattice mismatch and the mass difference between Si core and the shell layers. It should be pointed out that, the VDOS can only provide a qualitative analysis of the vibrations in the core–shell structure. Quantitative comparison of thermal conductivity of different core–shell nanowires should be accomplished using a phonon mode analysis.

Furthermore, we considered two more shell structures, SiO<sub>2</sub> and Si<sub>3</sub>N<sub>4</sub>, both of which are easily realized in experiments by oxidizing or nitriding the surface of a pure Si nanowire. The results are also reported in Fig. 7. Both core–shell structures achieved a large reduction of the thermal conductivity for the Si core as compared to pure Si NW. Especially for the Si-core/SiO<sub>2</sub>-shell nanowire, the reduction percentage is as high as 82%. We also calculated the size effect of the thermal conductivity of Si-core/SiO<sub>2</sub>-shell nanowire, as shown in Fig. 9. The MD results are fitted according to the following equation [32]:

$$\frac{1}{\kappa} = \frac{1}{\kappa_{\infty}^{NW}} \left( \frac{l_{NW}}{L_Z} + 1 \right) \quad (5)$$

where  $\kappa$  and  $L_Z$  are the thermal conductivity and the length of the nanowire, respectively,  $\kappa_{\infty}^{NW}$  is the thermal conductivity of an infinitely long nanowire, and  $l_{NW}$  is the effective phonon mean free path in the nanowire. The fitting yields  $\kappa_{\infty}^{NW} = 35$  W/mK for pure Si NW for interatomic potential [12] and  $\kappa_{\infty}^{Core} = 4.34$  W/mK for the Si core in core–shell nanowire. In the limit of infinite length, the reduction percentage of the thermal conductivity for the Si core in Si-core/SiO<sub>2</sub>-shell nanowire is 87.6%.

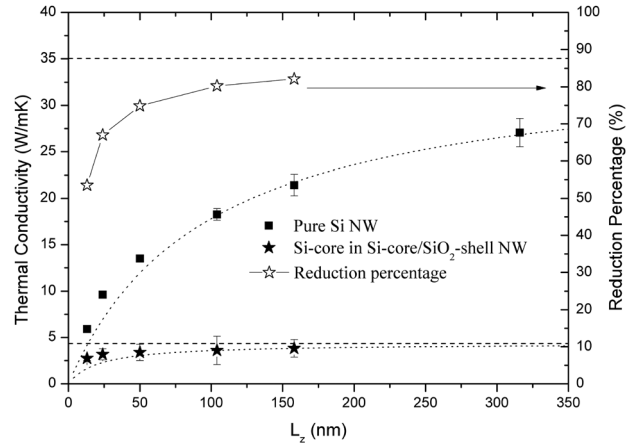


**Fig. 9 Calculated thermal conductivity of Si-core/SiO<sub>2</sub>-shell nanowire versus nanowire length at 300 K with comparison to that of a pure Si nanowire. The right axis is the reduction percentage of the thermal conductivity of the Si-core relative to that of the pure Si nanowire, as indicated by the arrow. The dotted lines are fitting to the MD results and the dashed lines denote the upper limit of the thermal conductivity of an infinitely long Si nanowire with same cross-sectional size.**

## 4 Conclusions

Nonequilibrium molecular dynamics simulations were performed to investigate three ways for reducing the thermal conductivity of nanowires: (1) surface roughening, (2) nanoparticle inclusions, and (3) surface coatings. Parameters considered include: the surface coverage and configuration of external particles, the different types of internal inclusions, and the different shell coatings. As compared to pristine nanowires, all modified nanocomposites were found to have considerably lower thermal conductivity.

Specifically, pure W nanoparticles sputtered onto a smooth Si nanowire surface (regularly or randomly) introduce surface roughness thereby reducing the thermal conductivity of the Si nanowire by up to 70%. The magnitude of the reduction becomes more significant with increasing particle number density but it appears to be rather independent of the distribution of the particles on the nanowire surface.

In addition, it was found that small numbers of Ge nanoparticles, with volumetric concentration less than 4%, distributed in the Si nanowire as inclusions result in significant scattering of propagating phonons and a concomitant reduction in the thermal conductivity of the nanowire by up to 70%. The magnitude of the reduction is not sensitive to the difference in atom mass or the interaction strength between inclusions and matrix.

Finally, surface coatings on Si nanowires [42] were found to create a larger reduction in thermal conductivity in comparison to the other methods. This result, we hypothesize, may originate from interfacial interference. Further evidence on the nature of this interference needs to be gathered in the future for a definitive statement to this end. Among the coatings simulated, GaN shows the best performance as compared to crystalline AlN, crystalline SiC and amorphous SiC. Remarkably, only two GaN layers can lower the thermal conductivity of Si nanowire by up to 78%. This reduction is attributed to the strong interfacial interaction strength and large atomic mass difference between the Si core and GaN shell. Even larger reduction in thermal conductivity of the Si core is achieved with amorphous SiO<sub>2</sub> and Si<sub>3</sub>N<sub>4</sub> shells. For example, a 160-nm-long Si nanowire coated with SiO<sub>2</sub> exhibits a reduction of 82%. By extrapolating these results to an infinitely long nanowire, we believe that the reduction can be as high as 87.6%. Moreover, a theoretical study [43] showed that electron mobility in silicon nanowires at room temperature can be greatly enhanced by embedding the nanowires within a hard material, making the

core-shell nanowire a very promising candidate for high  $ZT$  thermoelectrics.

## Acknowledgment

K.P.G. expresses his gratitude to ETH Zurich for a visiting professorship grant. X.Z. is grateful for a scholarship from the State Scholarship Fund of the China Scholarship Council that allowed him to be a visiting student at ETH Zurich and to contribute to this work. Computational support from the Brutus Cluster at ETH Zurich and Supercomputing Center of CAS in China is also gratefully acknowledged. This work was supported by a grant from the Swiss National Supercomputing Centre (CSCS) under project ID s243 and s359.

## Nomenclature

$A, B$  = parameters in Tersoff potential  
 $f$  = atomic force, eV/Å  
 $J_L$  = longitudinal heat flux, W/m<sup>2</sup>  
 $L$  = length, Å  
 $l$  = phonon mean free path, Å  
 $N$  = total number of atoms  
 $m, n$  = number of unit cells  
 $p_\lambda$  = participation ratio  
 $R$  = cutoff distance, Å  
 $r$  = atomic position, Å  
 $T$  = temperature, K  
 $V$  = volume of nanowire, Å<sup>3</sup>  
 $v$  = atomic velocity, Å/ps  
 $\varepsilon$  = local site energy of atoms, eV  
 $\omega$  = frequency, THz  
 $\delta, \beta, \eta$  = parameters in Tersoff potential  
 $\kappa$  = thermal conductivity, W/mK

## References

- [1] Majumdar, A., 2004, "Thermoelectricity in Semiconductor Nanostructures," *Science*, **303**, pp. 777–778.
- [2] Li, D., Wu, Y., Kim, P., Shi, L., Yang, P., and Majumdar, A., 2003, "Thermal Conductivity of Individual Silicon Nanowires," *Appl. Phys. Lett.*, **83**, pp. 2934–2936.
- [3] Hochbaum, A. I., Chen, R., Delgado, R. D., Liang, W., Garnett, E. C., Najarian, M., Majumdar, A., and Yang, P., 2008, "Enhanced Thermoelectric Performance of Rough Silicon Nanowires," *Nature*, **451**, pp. 163–167.
- [4] Chen, X., Wang, Y., and Ma, Y., 2010, "High Thermoelectric Performance of Ge/Si Core-Shell Nanowires: First-Principles Prediction," *J. Phys. Chem. C*, **114**, pp. 9096–9100.
- [5] Peng, K., Wang, X., Wu, X., and Lee, S., 2009, "Platinum Nanoparticle Decorated Silicon Nanowires for Efficient Solar Energy Conversion," *Nano Lett.*, **9**, pp. 3704–3709.
- [6] Yang, N., Zhang, G., and Li, B., 2008, "Ultralow Thermal Conductivity of Isotope-Doped Silicon Nanowires," *Nano Lett.*, **8**, pp. 276–280.
- [7] Hu, M., Giapis, K. P., Goicochea, J. V., Zhang, X., and Poulidakos, D., 2011, "Significant Reduction of Thermal Conductivity in Si/Ge Core-Shell Nanowires," *Nano Lett.*, **11**, pp. 618–623.
- [8] Hu, M., Zhang, X., Giapis, K. P., and Poulidakos, D., 2011, "Thermal Conductivity Reduction in Core-Shell Nanowires," *Phys. Rev. B*, **84**, p. 085442.
- [9] Yang, Z., Guarin, F., Tao, I. W., Wang, W. I., and Iyer, S. S., 1995, "Approach to Obtain High Quality GaN on Si and SiC-on-Silicon-on-Insulator Compliant Substrate by Molecular-Beam Epitaxy," *J. Vac. Sci. Technol. B*, **13**, pp. 789–791.
- [10] Schenk, H. P. D., Kipshidze, G. D., Lebedev, V. B., Shokhovets, S., Goldhahn, R., Kräußlich, J., Fissel, A., and Richter, W., 1999, "Epitaxial Growth of AlN and GaN on Si(1 1 1) by Plasma-Assisted Molecular Beam Epitaxy," *J. Cryst. Growth*, **201/202**, pp. 359–364.
- [11] Joblot, S., Semond, F., Natali, F., Vennéguès, P., Lügt, M., Cordier, Y., and Massies, J., 2005, "Growth of Wurtzite-GaN on Silicon (100) Substrate by Molecular Beam Epitaxy," *Phys. Status Solidi*, **2**, pp. 2187–2190.
- [12] Kumagai, T., Izumi, S., Hara, S., and Sakai, S., 2007, "Development of Bond-Order Potentials That Can Reproduce the Elastic Constants and Melting Point of Silicon for Classical Molecular Dynamics Simulation," *Comput. Mater. Sci.*, **39**, pp. 457–464.
- [13] Juslin, N., Erhart, P., Träskelin, P., Nord, J., Henriksson, K. O. E., Nordlund, K., Salonen, E., and Albe, K., 2005, "Analytical Interatomic Potential for Modeling Nonequilibrium Processes in the W–C–H System," *J. Appl. Phys.*, **98**(12), p. 123520.

- [14] Tersoff, J., 1989, "Modeling Solid-State Chemistry: Interatomic Potentials for Multicomponent Systems," *Phys. Rev. B*, **39**, pp. 5566–5568.
- [15] Stillinger, F. H., and Weber, T. A., 1985, "Computer Simulation of Local Order in Condensed Phases of Silicon," *Phys. Rev. B*, **31**, pp. 5262–5271.
- [16] Ding, K., and Anderson, H. C., 1986, "Molecular-Dynamics Simulation of Amorphous Germanium," *Phys. Rev. B*, **34**, pp. 6987–6991.
- [17] Karimi, M., Kaplan, T., Mostoller, M., and Jesson, D. E., 1993, "Ge Segregation at Si-Ge (001) Stepped Surfaces," *Phys. Rev. B*, **47**, pp. 9931–9932.
- [18] Erhart, P., and Albe, K., 2005, "Analytical Potential for Atomistic Simulations of Silicon, Carbon, and Silicon Carbide," *Phys. Rev. B*, **71**, p. 035211.
- [19] Nord, J., Albe, K., Erhart, P., and Nordlund, K., 2003, "Modelling of Compound Semiconductors: Analytical Bond-Order Potential for Gallium, Nitrogen and Gallium Nitride," *J. Phys.: Condens. Matter*, **15**, pp. 5649–5662.
- [20] Zhou, X. W., and Jones, R. E., 2011, "Effects of Cutoff Functions of Tersoff Potentials on Molecular Dynamics Simulations of Thermal Transport," *Modelling Simul. Mater. Sci. Eng.*, **19**, p. 025004.
- [21] Benkabou, F., Certier, M., and Aourag, H., 2003, "Elastic Properties of Zinc-Blende GaN, AlN and InN From Molecular Dynamics," *Mol. Simul.*, **29**, pp. 201–209.
- [22] Goumri-Said, S., Kanoun, M. B., Merad, A. E., Merad, G., and Aourag, H., 2004, "Prediction of Structural and Thermodynamic Properties of Zinc-Blende AlN: Molecular Dynamics Simulation," *Chem. Phys.*, **302**, pp. 135–141.
- [23] Munetoh, S., Motooka, T., Moriguchi, K., and Shintani, A., 2007, "Interatomic Potential for Si–O Systems Using Tersoff Parameterization," *Comput. Mater. Sci.*, **39**, pp. 334–339.
- [24] Billeter, S. R., Curioni, A., Fischer, D., and Andreoni, W., 2006, "Ab Initio Derived Augmented Tersoff Potential for Silicon Oxynitride Compounds and Their Interfaces With Silicon," *Phys. Rev. B*, **73**, p. 155329.
- [25] Billeter, S. R., Curioni, A., Fischer, D., and Andreoni, W., 2009, "Erratum: Ab Initio Derived Augmented Tersoff Potential for Silicon Oxynitride Compounds and Their Interfaces With Silicon [Phys. Rev. B **73**, 155329 (2006)]," *Phys. Rev. B*, **79**, p. 169904.
- [26] Ippolito, M., and Meloni, S., 2011, "Atomistic Structure of Amorphous Silicon Nitride From Classical Molecular Dynamics Simulations," *Phys. Rev. B*, **83**, p. 165209.
- [27] Plimpton, S., 1995, "Fast Parallel Algorithms for Short-Range Molecular Dynamics," *J. Comput. Phys.*, **117**, pp. 1–19.
- [28] Nosé, S., 1984, "A Unified Formulation of the Constant Temperature Molecular Dynamics Methods," *J. Chem. Phys.*, **81**, pp. 511–519.
- [29] Hoover, W. G., 1985, "Canonical Dynamics: Equilibrium Phase-Space Distributions," *Phys. Rev. A*, **31**, pp. 1695–1697.
- [30] Jund, P., and Julien, R., 1999, "Molecular Dynamics Calculation of the Thermal Conductivity of Vitreous Silica," *Phys. Rev. B*, **59**, pp. 13707–13711.
- [31] Müller-Plathe, F., 1997, "A Simple Nonequilibrium Molecular Dynamics Method for Calculating the Thermal Conductivity," *J. Chem. Phys.*, **106**(14), pp. 6082–6085.
- [32] Schelling, P. K., Phillpot, S. R., and Keblinski, P., 2002, "Comparison of Atomic-Level Simulation Methods for Computing Thermal Conductivity," *Phys. Rev. B*, **65**, p. 144306.
- [33] Pan, L., Lew, K. K., Redwing, J. M., and Dickey, E. C., 2005, "Stranski-Krastanov Growth of Germanium on Silicon Nanowires," *Nano Lett.*, **5**, pp. 1081–1085.
- [34] Hu, M., Goicochea, J. V., Michel, B., and Poulidakos, D., 2010, "Water Nanofilm-Induced Thermal Enhancement at Hydrophilic Quartz Interfaces," *Nano Lett.*, **10**, pp. 279–285.
- [35] Goicochea, J. V., Hu, M., Michel, B., and Poulidakos, D., 2011, "Surface Functionalization Mechanisms of Enhancing Heat Transfer at Solid-Liquid Interfaces," *ASME J. Heat Transfer*, **133**, p. 082401.
- [36] Hu, M., Zhang, X., Poulidakos, D., and Grigoropoulos, C. P., 2011, "Large 'Near Junction' Thermal Resistance Reduction in Electronics by Interface Nanoengineering," *Int. J. Heat Mass Transfer*, **54**, pp. 5183–5191.
- [37] Bell, R. J., and Dean, P., 1970, "Atomic Vibrations in Vitreous Silica," *Discuss. Faraday Soc.*, **50**, pp. 55–61.
- [38] Daly, B. C., Maris, H. J., Imamura, K., and Tamura, S., 2002, "Molecular Dynamics Calculation of the Thermal Conductivity of Superlattices," *Phys. Rev. B*, **66**, p. 024301.
- [39] Landry, E. S., and McGaughey, A. J. H., 2009, "Effect of Interfacial Species Mixing on Phonon Transport in Semiconductor Superlattices," *Phys. Rev. B*, **79**, p. 075316.
- [40] Termentzidis, K., Chantrenne, P., and Keblinski, P., 2009, "Nonequilibrium Molecular Dynamics Simulation of the In-Plane Thermal Conductivity of Superlattices With Rough Interfaces," *Phys. Rev. B*, **79**(21), p. 214307.
- [41] Termentzidis, K., Merabia, S., Chantrenne, P., and Keblinski, P., 2011, "Cross-Plane Thermal Conductivity of Superlattices With Rough Interfaces Using Equilibrium and Non-Equilibrium Molecular Dynamics," *Int. J. Heat Mass Transfer*, **54**, pp. 2014–2020.
- [42] Pokatilov, E. P., Nika, D. L., and Balandin, A. A., 2005, "Acoustic-Phonon Propagation in Rectangular Semiconductor Nanowires With Elastically Dissimilar Barriers," *Phys. Rev. B*, **72**, p. 113311.
- [43] Fonoberov, V. A., and Balandin, A. A., 2006, "Giant Enhancement of the Carrier Mobility in Silicon Nanowires With Diamond Coating," *Nano Lett.*, **6**, pp. 2442–2446.